PERGAMON

International Journal of Heat and Mass Transfer 43 (2000) 1141–1155

International Journal of HEAT and MASS TRANSFER

www.elsevier.com/locate/ijhmt

On capillary-driven flow and phase-change heat transfer in a porous structure heated by a finned surface: measurements and modeling

T.S. Zhao*, Q. Liao

Department of Mechanical Engineering, The Hong Kong University of Science and Technology, Clear Water Bay, Kowloon, Hong Kong

Received 18 August 1998; received in revised form 8 June 1999

Abstract

Characteristics of capillary-driven flow and phase-change heat transfer in a porous structure heated with a permeable heating source at the top were studied experimentally and theoretically in this paper. The experiments show that for small and moderate heat fluxes, the whole porous structure was fully saturated with liquid except adjacent to the horizontal heated surface where evaporation took place uniformly. For higher heat fluxes, a two-phase zone developed in the upper portion of the porous structure while the lower portion of the porous structure was saturated with subcooled liquid. When the imposed heat flux was further increased, a vapor blanket formed below the heated surface and the corresponding critical heat flux was reached. The heat transfer coefficient was modeled by simultaneously solving the problem of evaporating capillary meniscus in the pore level and the problem of fluid flow through a porous medium. The model is in good agreement with the experimental data, predicting the variations of the heat transfer coefficient with the increasing heating load.

1. Introduction

The subject of this paper is the study of capillary-driven heat and mass transfer in a porous structure heated with a permeable heating boundary at the top. Interest in this topic arose from the growing efforts on the development of capillary pumped loops (CPL) and loop heat pipes (LHP) which have many engineering applications including the thermal management of advanced space platforms and military spacecraft [1,2] as well as the cooling of electrical and electronic devices [3,4]. Unlike the previous problems involving phase-change heat transfer in a porous medium subjected to forced or natural convection [5–10], the capillary force in the present problem, developed at the liquid–vapor interface in the porous medium, is the sole driving-force of the flow motion. Another unique feature of the present problem is that the heating boundary is a periodically bounded one (with a number of fins) which permits the vapor leaving the heating boundary through the open space.

Although the experimental data on the present topic is scarce, some relevant theoretical and numerical investigations have been reported in the literature. Demidov and Yatsenko [11] numerically investigated the heat and mass transfer processes during evaporation in a wet capillary structure with a rectangular

* Corresponding author. Tel.: +852-2358-8647; fax: +852-2358-1543.

E-mail address: metzhao@ust.hk (T.S. Zhao)

0017-9310/0/$ - see front matter
PII: S0017-9310(99)00206-9

Nomenclature

A	dispersion constant
A_s	cross-sectional area of a cylindrical pore, m^2
c_p	specific heat, W/kg K
d_p	particle diameter of porous structure, m
g	gravity acceleration, m/s^2
h	heat transfer coefficient, W/m^2 K
h_{fg}	latent heat of vaporization, J/kg
K	permeability, m^2
K_c	curvature of liquid film, m^{-1}
k_l	thermal conductivity of liquid, W/m K
K_{rl}	liquid relative permeability
K_{rv}	vapor relative permeability
L	height of porous structure, m
L_s	height of subcooled liquid phase zone, m
$\dot{m}$	mass flux of liquid at the inlet of porous structure, kg/m^2 s
$\dot{m}_l$	total liquid mass flux in the two-phase zone, kg/m^2 s
$\dot{m}_v$	vapor mass flux departed through the fins, kg/m^2 s
$\dot{m}_{vr}$	re-circulated vapor mass flux, kg/m^2 s
p	pressure, Pa
p_c	capillary force, Pa
$p_d(\eta)$	disjoining pressure, Pa
q''	heat flux, kW/m^2
q''_{cr}	critical heat flux, kW/m^2
q''_{pk}	peak heat flux, kW/m^2
Q_p	total heat flow rate through a cylindrical pore, kW
$r(\eta)$	radius of liquid–vapor interface in pore, m
r_{eff}	effective pore radius, m
r_{men}	radius of the liquid meniscus, m
R_g	gas constant, J/kg k
s	scaled liquid saturation
s_l	liquid phase saturation
s_{li}	liquid phase irreducible saturation
s_{vi}	vapor phase irreducible saturation
T	temperature, °C
u	superficial velocity, m/s
x	coordinate of x-axis

Greek symbols

α	accommodation coefficient
$\delta_l(\eta)$	thickness of liquid film normal to pore wall, m
δ_0	thickness of the equilibrium non-evaporating liquid film, m
ε	porosity
η	coordinate along the solid–liquid interface
η_b	at the bottom of the liquid film meniscus in a cylindrical pore
η_0	the thickness of the equilibrium non-evaporating liquid film
μ	dynamic viscosity, m^2/s
ν	kinematics viscosity, kg/m s
θ	effective contact angle, degree
ρ	density, kg/m^3
σ	surface tension, N/m

Subscripts

f	front of the subcooled liquid zone
l	liquid
li	inlet of the porous structure
lv	liquid–vapor phase zone
max	maximum value
min	minimum value
s	saturation state
top	the top of porous structure
v	vapor
vo	outlet of vapor
wp	solid wall of a cylindrical pore
δ	liquid–vapor interface in pore

grooved heated wall. They formulated the problem based on two important assumptions. First, they assumed that there existed a superheated vapor zone in the vicinity of the heated wall (the groove tip) while the wick was saturated by a subcooled liquid elsewhere. Based on this assumption, Darcy's law was applied to the vapor zone and the liquid zone, respectively. They further assumed that, when the vapor zone did not exceed the heated surface, there would be a liquid meniscus near the corners formed by the lateral sides of the fin of the heating block and the top surface of the porous structure. On the other hand, when the vapor zone expanded beyond the surface of the heated wall, this liquid meniscus would disappear. They presented the patterns of isotherms and concluded that the critical heat flux was reached when the expansion of the vapor zone exceeded the area of the heated surface. Khrustalev and Faghri [12] numerically studied the heat and mass transfer processes around a heated triangular solid fin penetrating into a wetted porous structure. They also assumed that the heated surface was surrounded by a vapor zone. They concluded that the critical heat flux for this particular configuration was reached when the increase of the thermal resistance between the heated surface of the fin and the liquid zone with increasing heat flux reached an unac-

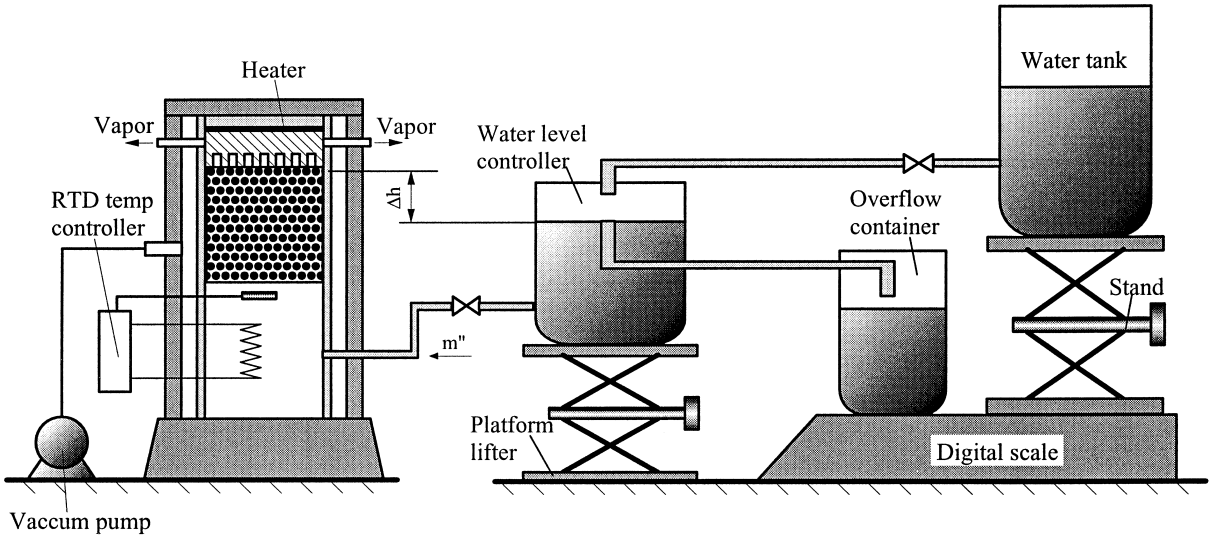

Fig. 1. Schematic of the experimental apparatus.

ceptable level or when the thickness of vapor zone at the fin top was equal to the minimum thickness of the porous structure.

In this paper, a combined experimental and theoretical study was carried out to investigate the capillary-driven heat and mass transfer characteristics of water flowing through a vertical rectangular packed-glass-bead structure heated by a finned wall at the top. First, we measured the heat transfer rates between the heating block and the porous structure and observed the phase-change behaviors occurring in the porous structure for different heat loads. Based on the experimental investigations, we then modeled the heat and mass transfer processes in such a system. It is shown that the predicted results are in good agreement with the experimental data.

In the following, we shall first report our experimental work on the problem under consideration. We shall then present a one-dimensional analysis to the problem based on thin liquid film evaporation in the pore level and liquid flow through a porous medium. Finally, the salient findings of the study will be summarized.

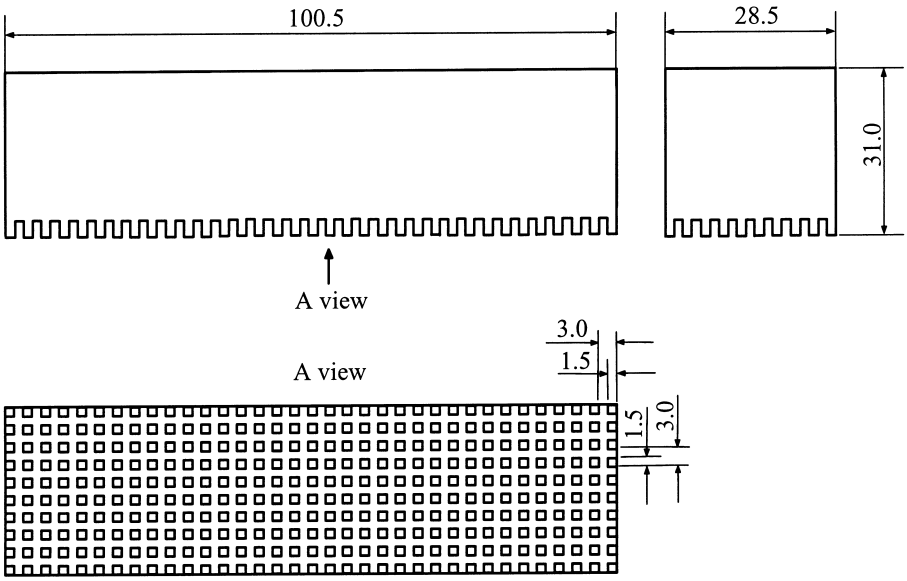

Fig. 2. Fined heating copper block.

2. Experimental study

2.1. Apparatus and procedures

Fig. 1 illustrates a schematic of the experimental apparatus used in the present investigation. The vertically-oriented test section (40 mm in height, 99 mm in width, and 29 mm in depth) was packed with glass beads, essentially spherical in shape, having an average particle diameter of $d_p = 1.09$ mm. The phase-change behavior within the porous structure could be observed through the transparent front plate. A finned copper block (shown in Fig. 2) with a stainless steel film (0.1 mm in thickness) serving as a heater, a mica sheet serving as an electrical insulator, and a Teflon cover plate serving as a heat insulator on the top, was placed on the top of the porous structure. As shown in Fig. 2, the extruded fin tips in the heating block were essentially flat in shape, with a rather small contact area (1.5×1.5 mm). The heating unit was carefully mounted on the top of the porous structure such that the fins of the heating block were in good contact with the porous medium. Both the top and the bottom boundaries of the test section were insulated using glass fiber wool while the vertical boundaries were well insulated by a vacuum vessel made of Plexiglas plates. The vacuum status was kept by a vacuum pump during the experiments. The inlet temperature of fluid was well controlled by a RTD temperature controller with two 50 W heaters located in the lower portion of the test section. The adverse hydrostatic head Δh (the distance between the top of the porous structure and the water level) was controlled by adjusting the elevation of the platform lifter, on which a water-level controller was placed. A RTD controller with a 1.5 kW heater was installed to keep the fluid temperature in the water-level controller to a desired value. Both the water tank and the overflow container were placed on a digital scale such that the mass flow rate flowing to the test section could be measured by reading the mass change per unit time. Four T-type thermocouples of 0.8 mm in diameter were used to measure the temperatures of the heating block while eighteen T-type thermocouples of 0.8 mm in diameter were inserted in the porous medium for measuring temperature distributions in the porous structure. The vapor pressure p_{vo} in the heated fins was measured by a differential pressure transducer (Validyne, Model DP15) and a carrier demodulator (Validyne, Model CD15). A data acquisition system, consisting of a personal computer, an A/D converter board (MetraByte DAS-20), and two universal analog input multiplexers (MetraByte EXP-20), was employed to record the temperature measurements.

In the present study, the heat transfer coefficient is defined as

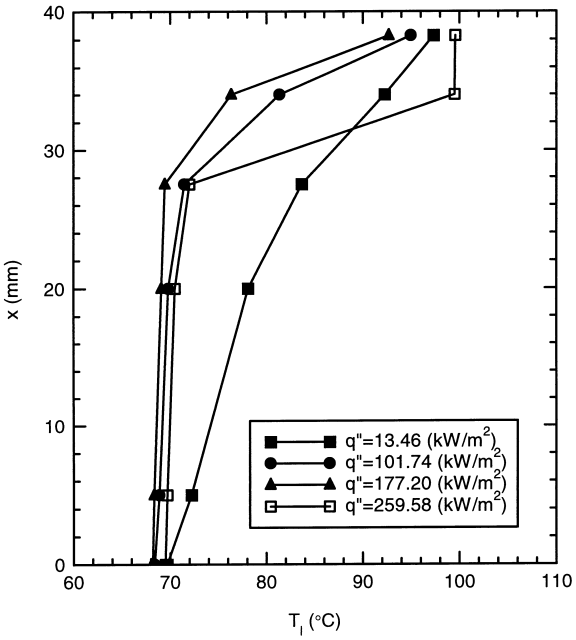

Fig. 3. Variations of the cross-sectional mean temperature along x-axis for different heat fluxes.

$$h = \frac{(Q - Q_{loss})}{A_h(\bar{T}_w - T_v)}, \tag{1}$$

where Q is the heating power, Q_{loss} is the heat loss, and A_h denotes the heating surface area, i.e., the cross-sectional area of the cooper block in contact with the porous medium. It was estimated that the heat loss was within 8% in the experiments. In Eq. (1), T_v is the saturated temperature corresponding to the pressure at exit p_{vo} while $\bar{T}_w$ is the mean temperature at the fin tips which was calculated by heat conduction using the measured temperatures in the heating block.

During the experiments, the adverse hydrostatic head was kept at $h = 35$ mm and the inlet temperature of the subcooled water at $T_{li} = 70°C$, while various heat fluxes were imposed. Under the steady-state condition for a specific heat flux, the mass flux of liquid, the outlet vapor pressure, as well as the temperatures in the heating block and the temperatures within the porous media were measured.

In this work the maximum capillary pressure (p_c)max of the porous structure was measured in a glass-bead packed tube according to the relation

$$(p_c)_{max} = \rho_l g L_{hu}, \tag{2}$$

where ρ_l is the density of the liquid water, and L_{hu} is the maximum static hold-up height, which was measured experimentally. The corresponding minimum liquid meniscus $(r_{men})_{min}$ and the minimum contact angle θ_{min} can be obtained from

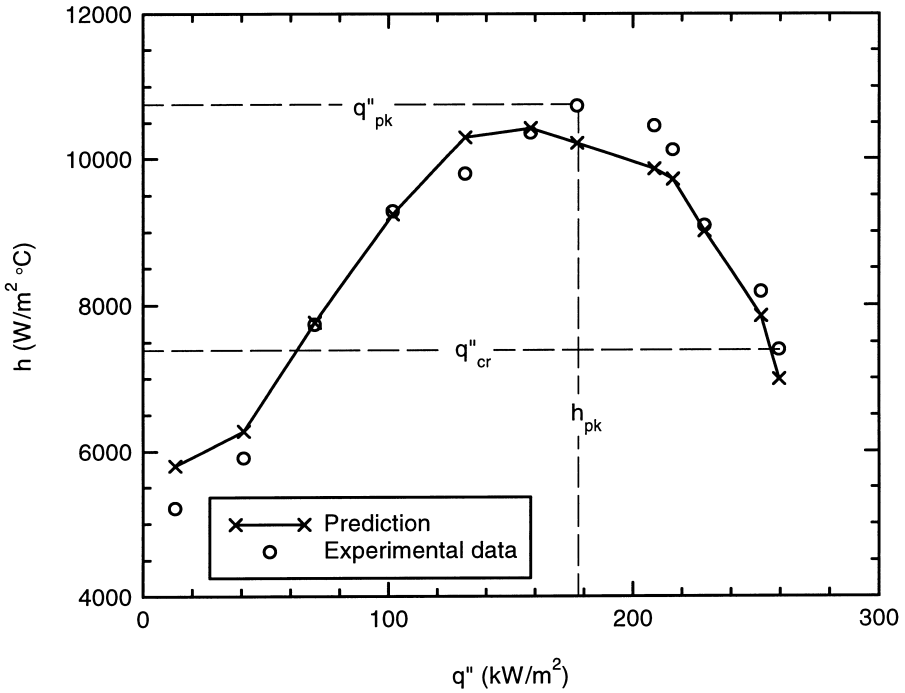

Fig. 4. Variation of the heat transfer coefficient versus the imposed heat flux.

$$(r_{\text{men}})_{\min} = \frac{2\sigma}{(p_c)_{\max}}, \tag{3}$$

and

$$(p_c)_{\max} = \frac{2\sigma \cos\theta_{\min}}{r_{\text{eff}}}, \tag{4}$$

where σ is the surface tension, and the effective pore radius r_{eff} is estimated by $r_{\text{eff}} = 0.21 d_p$ [4], with d_p being the diameter of the glass beads. From Eq. (3), we determine $(r_{\text{men}})_{\min} = 0.256$ mm for the present glass–water system.

2.2. Results

We now present the experimental results. The variations of the cross-sectional mean temperature along the x-axis at four heat fluxes of $q'' = 13.46$, 101.74, 177.20, and 259.58 kW/m^2 are illustrated in Fig. 3. For a small heat flux $q'' = 13.46$ kW/m^2), it is seen that the temperature rose almost lineally from the inlet zone toward the outlet of the porous structure. As the imposed heat flux was increased to $q'' = 101.74$ and 177.20 kW/m^2, however, the temperature variations (represented by the solid circles and the solid triangles in Fig. 3) along the x-axis in the lower portion of the porous structure became relatively small, but in the upper portion the temperature variation became extremely steep. This is because at a low heat flux only a small amount of water evaporated at the top of the porous structure and the induced mass flow rate of the working fluid was relatively small. Thus, the heat convection due to the corresponding movement of water was relatively insignificant for this case. However, as the heat flux was increased, more water evaporated and the motion of water in the porous medium became much more significant owing to a larger capillary-driven force developed at the liquid–vapor interface. Under this situation, heat transfer due to convection became more pronounced. Therefore, the temperatures increased relatively slowly in the lower portion of the porous wick evaporator due to the cooling effect of the subcooled water entering the structure from the bottom while it increased more rapidly in the upper portion of the porous structure because of the heating effect from the top of the structure. When the heat flux was increased to $q'' = 259.58$ kW/m^2, although the variation of the temperature in the lower portion of the porous structure was in close to that at $q'' = 177.20$ kW/m^2, the behavior was rather different in the vicinity of the heated surface: the temperatures at the two locations, $x = 34$ and 37.5 mm, were equal and at the saturated value. This clearly indicates that the two-phase zone existed adjacent to the heated surface when the imposed heat flux was sufficiently high.

We now present the measured heat transfer coefficient at various imposed heat fluxes in Fig. 4, where the circular symbols represent the measured data while

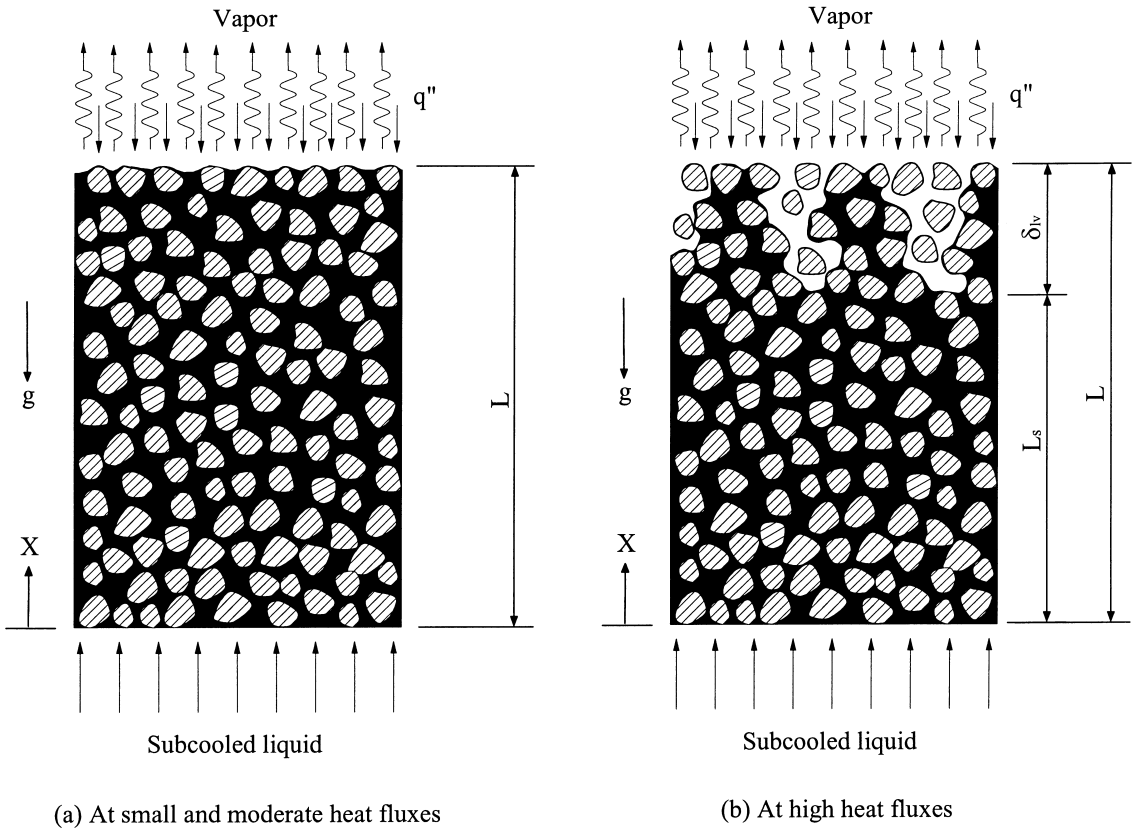

Fig. 5. Phase-change behaviors at different heat loads.

the solid line with cross symbols represents the theoretical prediction, which will be discussed in the later sections. It is shown that with an increase of heat flux, the heat transfer coefficient gradually increased, reached a peak value, and dropped rapidly afterwards. As illustrated in Fig. 4, this peak value will be referred to as the peak heat transfer coefficient hpk while the corresponding heat flux at which the peak heat transfer occurs will be referred to as the peak heat flux q''_{pk}. We now explain the variation of the heat transfer coefficient with the imposed heat flux based on our observations of the phase-change behavior occurring in the vicinity of the heated surface. During the experiments, we observed that the following three typical phase-change behaviors undergoing in the vicinity of the heated surface when the imposed heat flux is varied: (i) for heat fluxes smaller than the peak heat flux ($q''_{pk} = 177.2$ kW/m^2), no macroscopic vapor zone was visually observed. In this case, evaporation uniformly took place from the liquid residing on the heated surface of the porous structure while the reminder region of the porous structure was saturated with liquid, as sketched in Fig. 5a. The increase of the heat transfer coefficient with the imposed heat flux may be attributed to the fact that evaporating liquid film in the pore adjacent to the heated surface became thinner; (ii) as the imposed heat flux was larger than the peak value ($q''_{pk} = 177.2$ kW/m^2) but smaller than $q'' = 259.58$ kW/m^2, it was observed that vapor was formed in some locations along the heated surface and these local vapor zones receded downward into the porous structure while the reminder regions of the heated surface were still kept wetted, as sketched in Fig. 5b. In this case, heat transfer was primarily maintained by liquid evaporation in the reminder wetted regions. As the imposed heat flux was increased, the average area of the wetted region became smaller and therefore, the heat transfer coefficient began to drop with increasing heat flux; (iii) when the heat flux was varied further from $q'' = 259.58$ to 264.81 kW/m^2 (an increase of only 2%), a vapor blanket was formed along the heated surface of the porous structure. As a result, both the wall and the outlet temperatures increased drastically and the steady state could not be maintained. This is evident from Fig. 6 where the wall temperatures and the outlet vapor temperatures at $q'' = 259.58$ and 264.81 kW/m^2 are plotted against time. As seen from Fig. 6a and b, both the wall temperature and the outlet

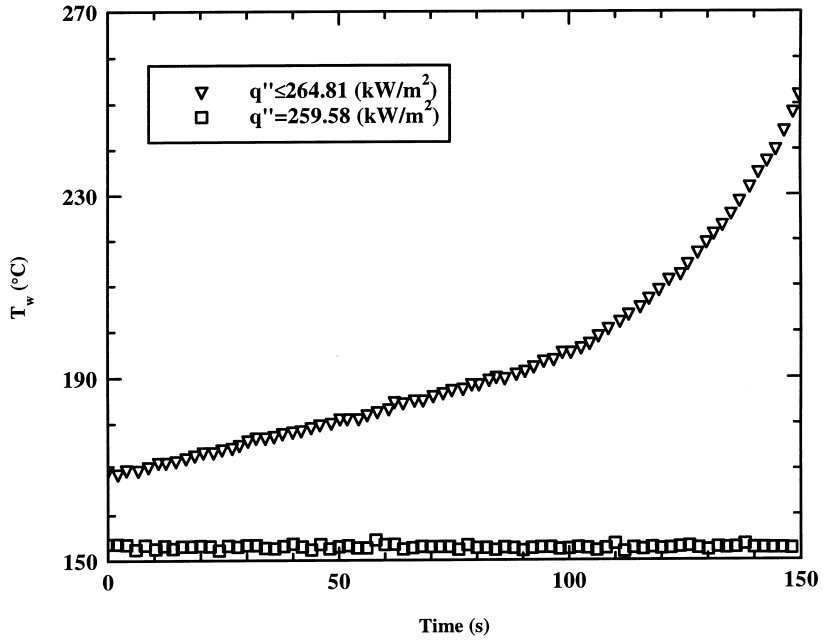

(a) Wall

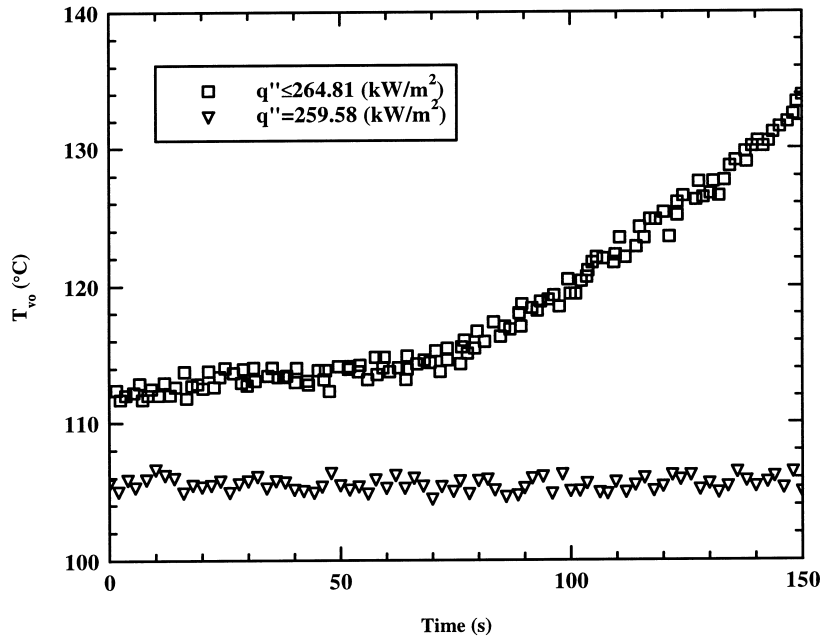

(b) Vapor

Fig. 6. Time-dependent wall and vapor temperatures at the critical heat flux.

temperature were independent of time when the imposed heat flux was kept at $q'' = 259.58$ kW/m^2. However, when the heat flux was increased to $q'' = 264.81$ kW/m^2, both the wall and the outlet temperatures increased exponentially with time. Therefore, the value of $q''_{cr} = 264.81$ kW/m^2 can be regarded as the critical heat flux under this particular condition.

The experimental findings can now be summarized as follows: (i) when $q'' < q''_{pk}$, the whole porous structure was fully saturated with liquid except the heated surface where liquid evaporation took place uniformly; (ii) in the range of $q''_{pk} < q'' < q''_{cr}$, a two-phase zone was formed in the vicinity of the heated surface; and (iii) at q''_{cr}, a vapor blanket formed below the heated surface and q''_{cr} was considered to be the corresponding critical heat flux.

3. Theoretical study

Based on the above experimental observations, we now model heat and mass transfer in a capillary structure heated by a permeable boundary at the top. We shall treat the following two cases separately: (i) the case of small and moderate heat fluxes ($q'' < q''_{pk}$), as depicted in Fig. 5a; and (ii) the case of higher heat fluxes ($q''_{pk} < q'' < q''_{cr}$), as depicted in Fig. 5b.

3.1. The case of small and moderate heat fluxes

In this section, we shall first analyze heat and fluid flow through a porous medium based on Darcy's law and then model heat and mass transfer in the pore level of the porous structure based on thin liquid film evaporation theory.

3.1.1. Liquid flow in a porous medium

We now consider macroscopic motion of liquid through a porous medium as shown in Fig. 5a. A one-dimensional approximation of force balance in the vertical direction yields

$$p_c = \Delta p_l + (p_{vo} - p_{li}) + \rho_l g L, \tag{5}$$

where the capillary force p_c is given by

$$p_c = \frac{2\sigma \cos\theta}{r_{eff}} = \frac{2\sigma}{r_{men}}. \tag{6}$$

Δp_l in Eq. (5) representing the pressure drop due to the liquid flow in the porous structure can be evaluated by Darcy's law as

$$\Delta p_l = \frac{\dot{m} \nu_l L}{K}, \tag{7}$$

where $\dot{m}$ is the mass flow rate of fluid, and $K = d_p^2 \varepsilon^3 / 150(1-\varepsilon)^2$ is the permeability of the porous structure, with ε being the porosity of the porous medium, and ν_l is the kinematic viscosity of liquid. The second term $(p_{vo} - p_{li})$ in Eq. (5) represents the pressure difference between the inlet and the outlet, which was obtained experimentally, as mentioned earlier. The third term in the right-hand side of Eq. (5), $\rho_l g L$, represents the adverse gravity. Substituting Eqs. (6) and (7) into Eq. (5) and rearranging yield

$$\frac{2\sigma}{r_{men}} = \frac{\dot{m} \nu_l L}{K} + (p_{vo} - p_{li}) + \rho_l g L. \tag{8}$$

Eq. (8) establishes the relationship between the capillary force and the pumped mass flux. In addition, the overall energy balance for the system requires

$$q'' = \dot{m} h_{fg} + \dot{m} c_{pl} (T_v - T_{li}), \tag{9}$$

where the first term on the right-hand side represents the latent heat, with h_{fg} being the latent heat of vaporization per unit mass, while the second term represents the sensible heat from the inlet to the outlet. It should be noted from Eq. (9) that the heat loss due to conduction from the bottom of the porous structure is neglected. This assumption can be justified in considering that: (i) the effective thermal conductivity of glass bead–water system is rather small (0.706 W/m °C); and (ii) the temperature gradient at this location is rather small as noted from the experimental data shown in Fig. 3. Combining Eqs. (8) and (9) gives

$$p_c = \frac{2\sigma}{r_{men}} = \frac{\nu_l L}{K} \frac{q''}{\left[h_{fg} + c_{pl}(T_v - T_{li})\right]} + (p_{vo} - p_{li}) + \rho_l g L. \tag{10}$$

Eq. (10) indicates that for a given heat flux q'', capillary menisci are established at the heated surface of the porous structure with a liquid meniscus radius r_{men}. These menisci facilitate the pumping function, which draws liquid from the wetted porous structure to the heated surface to be evaporated. Eq. (10) also shows that a larger heat flux will lead to a larger capillary force. However, it should be noted that in practice when the heat flux q'' is increased to a certain value, the liquid meniscus radius will reach the minimum value $(r_{men})_{min}$, or the equivalent capillary force reaches its maximum value $(p_c)_{max}$. It is of significance to find out the value of the heat flux at which the capillary force reaches its maximum value $(p_c)_{max}$. To this end, we substitute the measured peak heat flux $q''_{pk} = 177.2$ kW/m^2 and the corresponding p_{vo} listed in Table 2 into Eq. (10), we obtain $(r_{men})_{min} = 0.252$ mm. This value is almost the same as the measured $(r_{men})_{min} = 0.256$ mm as discussed earlier. This implies that at $q''_{pk} = 177.2$ kW/m^2 the capillary force reaches its

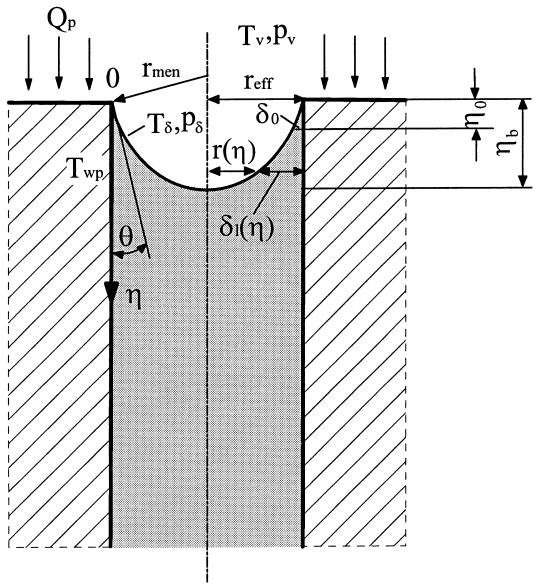

Fig. 7. Heat transfer in the pore level.

maximum value $(p_c)_{max}$. Therefore, a further heat addition will not lead to a larger pumping action. Conversely, the increase of the imposed heat flux will cause more vapor produced at the top of the porous structure. As a result, a two-phase zone may exist at the top of the porous structure and the heat transfer coefficient begins to drop after q_{pk}. This analysis is consistent with experimental observations.

3.1.2. Heat transfer in a pore

As mentioned previously, for small and moderate heat fluxes, evaporation took place uniformly on the heated surface at the top of the porous structure, as depicted in Fig. 5a. Following Khrustalev and Faghri [12], we idealize the problem of evaporative heat transfer of liquid in the pore level of porous media to a problem of heat conduction through the capillary meniscus with a radius rmen situated in a cylindrical pore with an effective pore radius r_{eff}, as shown in Fig. 7. For the present experiment with $d_p = 1.09$ mm, the effective pore radius $r_{eff} = 0.21 d_p = 0.229$ mm while the capillary meniscus radius r_{men} is obtained from Eq. (10). The major assumptions of the analysis of heat transfer in the pore level include [12]: (i) the temperature of the solid–liquid interface T_{wp} is constant along the η-coordinate for a small radius of the capillary meniscus; (ii) vapor at the exit is in the saturated state; and (iii) the curvature of the axisymmetrical liquid meniscus is estimated by $2/r_{men}$ and hence is independent of η. If we further assume that the heat conduction through the liquid film is one-dimensional and normal to the wall of the pore wall, we can write the local heat flux q''_l through the liquid film as

$$q''_l(\eta) = k_l \frac{T_{wp} - T_\delta(\eta)}{\delta_l(\eta)}, \tag{11}$$

where the local liquid film thickness $\delta_l(\eta)$, as shown in Fig. 7, is geometrically related to the effective radius r_{eff} and the capillary meniscus radius r_{men} by

$$\delta_l(\eta) = r_{eff} - \sqrt{r_{men}^2 - \left(\sqrt{r_{men}^2 - r_{eff}^2} + \eta\right)^2}. \tag{12}$$

In Eq. (11), $T_\delta(\eta)$ is the temperature at the liquid film free surface, which is affected by the disjoining pressure p_d and the capillary pressure p_c, and also depends on the interfacial thermal resistance for an extremely thin liquid film in the pore. The heat flux $q''_\delta(\eta)$ due to evaporation at the liquid–vapor interface can be obtained from [13]

$$q''_\delta(\eta) = -\left(\frac{2\alpha}{2-\alpha}\right)\frac{h_{fg}}{\sqrt{2\pi R_g}}\left[\frac{p_s(T_v)}{\sqrt{T_v}} - \frac{p_\delta(\eta)}{\sqrt{T_\delta(\eta)}}\right], \tag{13}$$

where $\alpha = 0.3$ is the accommodation coefficient for water [13], R_g is the gas constant, and $p_s(T_v)$ represents the saturation pressure corresponding to the vapor temperature T_v. The pressure at the thin film interface $p_\delta(\eta)$ in Eq. (13) can be obtained by the extended Kelvin equation [13]

$$p_\delta(\eta) = p_s(T_\delta)\exp\left[\frac{p_\delta(\eta) - p_s(T_\delta) + p_d(\eta) - \sigma K_c}{\rho_l R_g T_\delta(\eta)}\right], \tag{14}$$

where $p_s(T_\delta)$ represents the saturation pressure corresponding to the temperature at the liquid film interface T_δ, $K_c = 2/r_{men}$ is the curvature of the liquid–vapor interface, and the disjoining pressure $p_d(\eta)$ is evaluated by [13]

$$p_d(\eta) = -\frac{A}{\delta_l(\eta)^3} \tag{15}$$

with $A = 3.11 \times 10^{-21}$ being the dispersion constant for water on the glass substrate [14].

Under steady-state conditions, the heat conduction through the liquid film $q''_l(\eta)$ is balanced by the evaporative heat transfer $q''_\delta(\eta)$ at the liquid–vapor interface, i.e: $q''_l(\eta) = q''_\delta(\eta)$. It follows from Eqs. (11) and (13) that

$$T_\delta(\eta) = T_{wp} + \frac{\delta_l(\eta)}{k_l}\left(\frac{2\alpha}{2-\alpha}\right)\frac{h_{fg}}{\sqrt{2\pi R_g}}$$

$$\left[\frac{p_s(T_v)}{\sqrt{T_v}} - \frac{p_\delta(\eta)}{\sqrt{T_\delta(\eta)}}\right]. \quad (16)$$

Thus, the interfacial temperature $T_\delta(\eta)$ and pressure $p_\delta(\eta)$ can be obtained by solving Eqs. (14) and (16) simultaneously for given values of T_v, T_{wp}, and $\delta_l(\eta)$.

As indicated from Eq. (15), the disjoining pressure increases when the liquid film becomes thin. Since the liquid film near the top of the pore ($\eta \to 0$) becomes extremely thin, the disjoining pressure in this region becomes rather high. As a result, the pressure $p_\delta(\eta)$ at the liquid film interface is much lower than the saturation pressure $p_s(T_v)$ corresponding to the vapor temperature T_v, thereby the thermal resistance at the liquid–vapor phase interface becoming very high. For this reason, a non-evaporating superheated liquid film exists in the extremely thin liquid film near the top of the pore. The thickness of the equilibrium non-evaporating liquid film 0 can be obtained from Eqs. (11) to (16) by letting $q''_\delta(\eta) = 0$, $T_\delta(\eta) = T_{wp}$, and $\delta_l(\eta) = \delta_0$ to give

$$\delta_0 = A^{1/3}\left\{p_s(T_v)\sqrt{\frac{T_{wp}}{T_v}} - p_s\left(T_{wp}\right) - \rho_l R_g T_{wp} \ln\left[\frac{p_s(T_v)}{p_s\left(T_{wp}\right)}\sqrt{\frac{T_{wp}}{T_v}}\right]\right\}^{-1/3}, \quad (17)$$

where $p_s(T_{wp})$ is the saturation pressure corresponding to the wall temperature T_{wp}. Note that the capillary force term is neglected due to $\sigma K_c < p_d$. The length of the equilibrium non-evaporating liquid film η_0 along the coordinate corresponding to δ_0 can be obtained from

$$\eta_0 = \sqrt{r_{men}^2 - (r_{eff} - \delta_0)^2} - \sqrt{r_{men}^2 - r_{eff}^2}. \quad (18)$$

Considering that the heat transfer takes place only from η_0 to $\eta_b = r_{men} - \sqrt{r_{men}^2 - r_{eff}^2}$ (see Fig. 7), the total heat flow rate through a single pore Q_p is defined as

$$Q_p = \int_{\eta_0}^{\eta_b} \frac{T_{wp} - T_\delta(\eta)}{\delta_l(\eta)} 2\pi r(\eta)\, d\eta, \quad (19)$$

where

$$r(\eta) = r_{eff} - \delta_l(\eta) = \sqrt{r_{men}^2 - \left(\sqrt{r_{men}^2 - r_{eff}^2} + \eta\right)^2}. \quad (20)$$

Under the assumption that the surface porosity of the porous structure equals to the volumetric porosity ε, the cross-sectional area of a cylindrical pore A_s can be represented by

$$A_s = \frac{\pi r_{eff}^2}{\varepsilon}. \quad (21)$$

The evaporative heat flux at the top of the porous structure Q_p/A_s is balanced by the latent heat of the incoming liquid flow $\dot{m}$, thus

$$Q_p = \frac{\dot{m} h_{fg} \pi r_{eff}^2}{\varepsilon}. \quad (22)$$

Combining Eqs. (19) and (22) yields

$$\frac{\dot{m} h_{fg} \pi r_{eff}^2}{\varepsilon} = \int_{\eta_0}^{\eta_b} \frac{T_{wp} - T_\delta(\eta)}{\delta_l(\eta)} 2\pi r(\eta)\, d\eta. \quad (23)$$

We now define the predicted heat transfer coefficient as

$$h_{pre} = \frac{q''}{T_{wp} - T_v}, \quad (24)$$

where the wall temperature T_{wp} can be obtained by solving Eqs. (16) and (23) simultaneously for a given imposed heat flux q''.

3.1.3. Summary

We now summarize the procedures of calculating heat transfer coefficient hpre for small and moderate heat fluxes presented above. For a given heat flux q'', the meniscus radius rmen of the liquid film can be determined from Eq. (10). The local liquid film thickness $\delta_l(\eta)$ in the cylindrical pore can then be determined from Eq. (12). T_{wp} and $T_\delta(\eta)$ can be obtained by solving Eqs. (16) and (23) simultaneously. The heat transfer coefficient h_{pre} can finally be calculated from Eq. (24).

3.2. The case of high heat fluxes

Fig. 5b depicts the induced flow in the porous structure at high heat fluxes. The induced flow can be divided into two zones: a two-phase zone with a length of δ_{lv} in the upper section and a subcooled liquid zone with a length of L_s in the lower portion. In the two-phase zone, the liquid saturation s varies from unity at the subcooled liquid front ($x = L_s$) to a value at the top ($x = L$), denoted by s_{top}, where $s_{top} < 1$. It is seen from Fig. 5b that the heated surface at $x = L$ consists of vapor regions and wetted regions, with s_{top} describing the relative fraction of the wetted regions. We now assume that in this case liquid evaporation takes place only on the wetted top surface and there is no evapor-

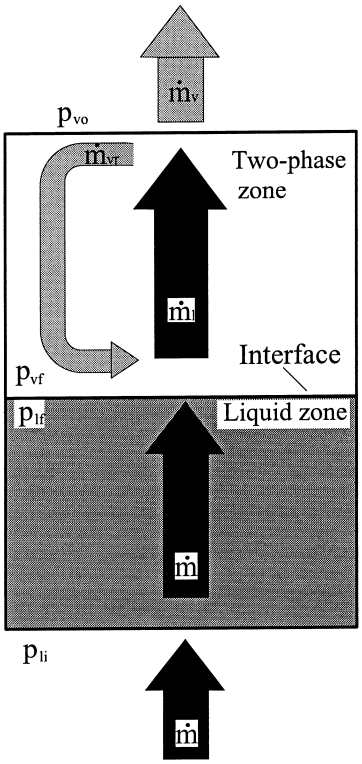

Fig. 8. Schematic of the re-circulated vapor mass flux in the two-phase zone.

ation inside the porous structure. This assumption is based on the fact that the isothermal two-phase zone in the top of the porous structure precludes heat conducted from the heated surface to the two-phase zone. The rapid evaporation on the wetted top surface at high heat fluxes leads to an increase vapor pressure at the heated surface. This, in turn, may cause some of generated vapor re-entering to the porous structure, due to a slight pressure gradient from the top toward bottom, although the majority of vapor moves out from the fins. This re-circulated vapor eventually condenses at the interface between the subcooled liquid and the two-phase zone ($x = L_s$). We now analyze the mass balance in the domain as illustrated in Fig. 8. If we denote the total evaporation mass flux or the total liquid flux in the two-phase zone moving toward the heated surface by $\dot{m}_l$, then we have the following mass balance at the heated surface

$$\dot{m}_l = \dot{m}_v + \dot{m}_{vr}, \tag{25}$$

where$\dot{m}_v$ is the vapor mass flux departed through the fins and $\dot{m}_{vr}$ represents the re-circulated vapor mass flux. Under the steady-state condition, the global mass conservation requires that the total subcooled liquid mass flux $\dot{m}$ equals to the vapor mass flux departed through the fins $\dot{m}_v$, thus $\dot{m}_v = \dot{m}$, where $\dot{m}$ is given by Eq. (9). The re-circulated vapor mass flux $\dot{m}_{vr}$ can be obtained from the energy balance as

$$\dot{m}_{vr} h_{fg} = \dot{m} c_{pl}(T_s - T_{li}). \tag{26}$$

Eq. (26) indicates that the increase of subcooled liquid temperature from the inlet toward the subcooled liquid front is due to the heat release from the re-circulated vapor condensation. Substituting Eq. (9) into Eq. (26) yields

$$\dot{m}_{vr} = \frac{q''}{h_{fg}/[c_{pl}(T_s - T_{li})] + 1}. \tag{27}$$

Introducing a dimensionless parameter φ

$$\varphi = \frac{\dot{m}_v}{\dot{m}_{vr}} = \frac{h_{fg}}{c_{pl}(T_s - T_{li})}. \tag{28}$$

Eqs. (26) and (27) can then be rewritten as

$$\dot{m}_{vr} = \frac{q''}{(1+\varphi)h_{fg}}, \tag{29}$$

and

$$\dot{m}_v = \frac{q''}{(1+1/\varphi)h_{fg}}. \tag{30}$$

We now assume that the heat flow rate through a single cylindrical wet pore can be written as

$$Q_p = \dot{m}_p h_{fg} A_s, \tag{31}$$

where $\dot{m}_p = \dot{m}_l / s_{top}$ is the mass flux of liquid flowing to the wetted pore, and the cross-sectional area of a cylindrical pore A_s is given by Eq. (21). Combining Eqs. (31) and (21) and with the aid of Eq. (19) gives the energy balance at the cylindrical pore as

$$\frac{\dot{m} h_{fg} \pi r_{eff}^2}{\varepsilon s_{top}} = \int_{\eta_0}^{\eta_b} \frac{T_{wp} - T_\delta(\eta)}{\delta_l(\eta)} 2\pi r(\eta)\, d\eta, \tag{32}$$

where the local liquid film thickness $\delta_l(\eta)$ in the cylindrical pore can then be determined from Eq. (12) for an appropriate capillary radius rmen. As discussed earlier, when the heat flux exceeds q''_{pk}, the capillary radius reduces to its minimum value $(r_{men})_{min}$ or the corresponding capillary force attends its maximum value $(p_c)_{max}$, which was experimentally determined from Eq. (3). It follows that the local liquid film thickness $\delta_l(\eta)$ at higher heat fluxes can be determined from Eq. (12). The mass flux $\dot{m}$ in Eq. (32) can be obtained from Eq. (9) for a specific heat flux while the other two unknowns T_{wp} and $T_\delta(\eta)$ can be obtained by solving Eqs. (16) and (32) simultaneously. The only remaining unknown in Eq. (32) is the saturation at the

heated surface s_{top}. To obtain s_{top}, we have to first obtain the length of the two-phase zone δ_{lv}.

3.2.1. Determination of the length of the two-phase zone δ_{lv}

We now consider the one-dimensional problem of fluid flow through the porous medium in the liquid zone ($0 \le x \le L_s$). The superficial velocity of fluid in the liquid zone is given by

$$u_l = -\frac{K}{\mu_l}\left(\frac{dp_l}{dx} + \rho_l g\right). \tag{33}$$

The boundary conditions for Eq. (33) are

$$\text{at } x = 0: \quad p_l = p_{li} \tag{34}$$

$$\text{at } x = L_s: \quad p_l = p_{lf} \tag{35}$$

where p_{lf} is the liquid pressure at the interface between the subcooled liquid zone and the two-phase zone ($x = L_s$), which is related to the vapor pressure p_{vf} and the capillary pressure by

$$p_{lf} = p_{vf} - (p_c)_{max}, \tag{36}$$

with the vapor pressure at $p_{vf}(x = L_s)$ being determined later by Eq. (52). The length of the two-phase zone δ_{lv} can be obtained by integrating Eq. (33) subjected to the boundary conditions Eqs. (34) and (35) to give

$$\delta_{lv} = L - L_s = L - \frac{\left[(p_c)_{max} - (p_{vf} - p_{li})\right]}{\left(\dot{m}\nu_l/K + \rho_l g\right)}. \tag{37}$$

3.2.2. Determination of the saturation at the top s_{top}

In this section, we shall conduct a one-dimensional hydrodynamic analysis to determine the saturation distribution in the two-phase zone. As discussed previously, a counter-current flow of the liquid phase $\dot{m}_l$ and the vapor phase $\dot{m}_{vr}$ exists in the two-phase zone. The pressure gradients of vapor phase and liquid phase can be given as, respectively,

$$\frac{dp_v}{dx} = -\frac{u_v \mu_v}{K K_{rv}} - \rho_v g, \tag{38}$$

and

$$\frac{dp_l}{dx} = -\frac{u_l \mu_l}{K K_{rl}} - \rho_l g, \tag{39}$$

where K_{rl} is the relative permeability of liquid phase with the subscripts 'l' and 'v' denoting the liquid phase and vapor phase, respectively. Rewriting Eqs. (38) and (39) in terms of the vapor mass flux and the liquid mass flux gives

$$\frac{dp_v}{dx} = \frac{\dot{m}_{vr}\nu_v}{K K_{rv}} - \rho_v g, \tag{40}$$

and

$$\frac{dp_l}{dx} = -\frac{\dot{m}_l \nu_l}{K K_{rl}} - \rho_l g. \tag{41}$$

Subtracting Eq. (40) from Eq. (41) gives the capillary pressure gradient in the two-phase zone as

$$\frac{dp_c}{dx} = \frac{\dot{m}_l \nu_l}{K K_{rl}} + \frac{\dot{m}_{vr}\nu_v}{K K_{rv}} + (\rho_l - \rho_v) g, \tag{42}$$

Substituting Eqs. (29) and (30) into Eq. (42) yields

$$\frac{dp_c}{dx} = \frac{q''}{K h_{fg}(1+\varphi)}\left[\frac{(1+\varphi)\nu_l}{K_{rl}} + \frac{\nu_v}{K_{rv}}\right] + (\rho_l - \rho_v) g. \tag{43}$$

We now define the following dimensionless parameters [15]

$$\xi = \frac{(x - L_s)(\rho_l - \rho_v) g}{\sigma}\left(\frac{K}{\varepsilon}\right)^{1/2}, \quad f = \frac{p_c}{\sigma}\left(\frac{K}{\varepsilon}\right)^{1/2},$$

$$\omega = \frac{q''\nu_v}{(1+\varphi) K h_{fg}(\rho_l - \rho_v) g}, \quad \beta = (1+\varphi)\frac{\nu_l}{\nu_v},$$

and

$$s = \frac{s_l - s_{li}}{1 - s_{li} - s_{vi}},$$

where s_{li} and s_{vi} represent the irreducible liquid and vapor saturation. Eq. (43) can then be recast into a dimensionless form

$$\frac{df}{d\xi} = \omega\left(\frac{1}{K_{rv}} + \frac{\beta}{K_{rl}}\right) + 1. \tag{44}$$

If it is assumed that the capillary pressure is a function only of s in the two-phase zone, then

$$\frac{df}{d\xi} = \frac{df}{ds}\frac{ds}{d\xi}. \tag{45}$$

It follows from Eqs. (44) and (45) that

$$\frac{ds}{d\xi} = \frac{\left[\omega\left(\frac{1}{K_{rv}} + \frac{\beta}{K_{rl}}\right) + 1\right]}{f'}. \tag{46}$$

An equation similar to Eq. (46) was also obtained by Undell [15]. The appropriate boundary condition of Eq. (46) at the interface between the subcooled liquid zone and the two-phase zone is

$$\xi = 0: \quad s = 1 \tag{47}$$

Table 1
Data for the computation of the presented example

Liquid	Water
Solid	Glass
Particle diameter of glass beads, d_p	1.09 (mm)
Porosity of the packed glass beads, ε	0.3685
Gas constant, R_g	462 (J kg^{-1} K^{-1})
Dispersion constant, A	3.15×10^{-21} J
Accomodation coefficient α	0.03
Irreducible liquid saturation, s_{li}	0
Irreducible vapor saturation, s_{vi}	0.11 (N m^{-1})
Surface tension σ	0.05886
Minimum effective contact angle θ_{min}	26.649 (degree)
Latent heat of evaporation, h_{fg}	2257.1×10^3 (J kg^{-1})
Density of saturation vapor, ρ_v	0.5977 (kg m^{-3})
Density of saturation liquid, ρ_l	998 (kg m^{-3})
Kinematic viscosity of liquid υ_l in liquid zone	3.26×10^{-7} (m^2 s^{-1})
Kinematic viscosity of liquid υ_l in two-phase zone	2.95×10^{-7} (m^2 s^{-1})
Thermal conductivity of solid, k_w	0.78 (W m^{-1} K^{-1})
Thermal conductivity of liquid, k_l	0.68 (W m^{-1} K^{-1})

The liquid and vapor relative permeabilities reported by Verma et al. [16] can be represented by the following expressions

$$K_{rl} = s^3, \tag{48}$$

and

$$K_{rv} = 1.2984 - 1.9832s + 0.7432s^2. \tag{49}$$

The correlation for capillary pressure data obtained by Grosser et al. [17] gives

$$f(s) = 0.48 + 0.036 \ln\left[\frac{(1 - s_l)}{s_l}\right]. \tag{50}$$

The scaled liquid saturation distribution in the two-phase zone can now be obtained by solving Eq. (46) subjected to the boundary condition Eq. (47) by the Runge–Kutta method for a specific heat flux q'' and the length of two-phase zone δ_{lv} given by Eq. (37). Thus, the saturation at the heated surface s_{top} can be determined.

Another unknown for solving the length of the two-phase zone δ_{lv} from Eq. (37) is the vapor pressure p_{vf} at the interface between the subcooled liquid zone and the two-phase zone ($x = L_s$), which can now be obtained by first substituting Eq. (29) into Eq. (38)), followed by integrating Eq. (38) subject to the boundary condition

$$x = L: \quad p_v = p_{vo} \tag{51}$$

to give

Table 2
Measured outlet pressures vs. predicted saturation and the length of the two-phase zone

Imposed heat flux (kW/m^2)	p_{vo} gauge pressure (Pa)	Predicted s ($X = 40$ mm)	Predicted δ_{lv} (mm)
13.5	6.21	1.000	0.00
41.01	21.13	1.000	0.00
69.94	61.56	1.000	0.00
101.74	92.53	1.000	0.00
131.46	107.41	1.000	0.00
158.25	113.79	0.998	0.85
177.19	124.64	0.973	1.24
208.75	139.51	0.927	2.82
216.35	143.72	0.911	3.26
229.24	161.11	0.835	5.09
252.23	182.73	0.711	7.37
259.58	195.12	0.628	8.68

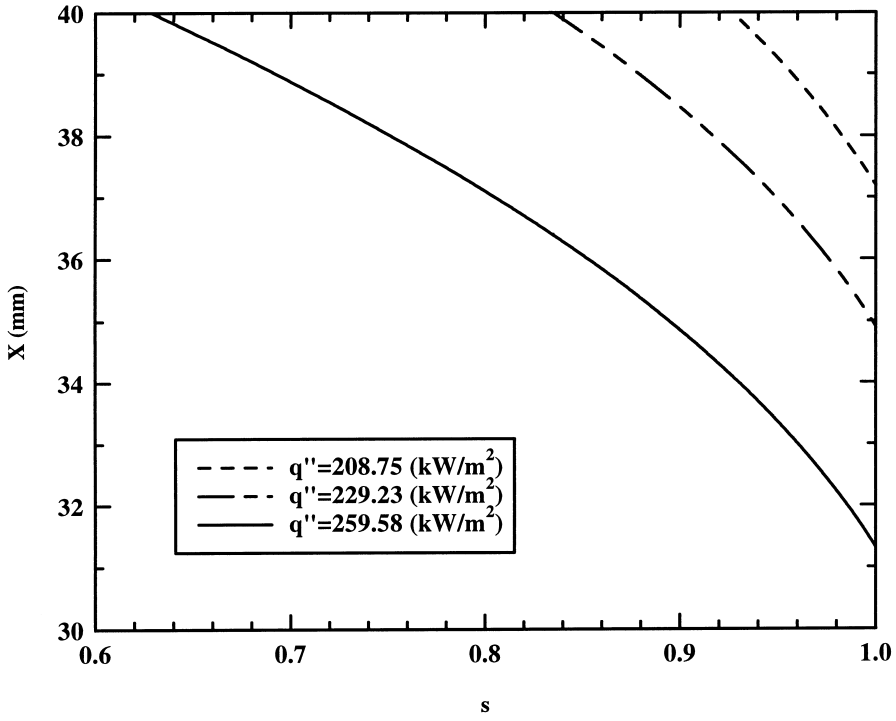

Fig. 9. Predicted saturation distributions for different heat fluxes.

$$p_{vf} = p_{vo} - \int_{L_s}^{L} \left[\frac{q'' \nu_v}{K h_{fg} (1+\varphi) K_{rv}} - \rho_v g \right] dx. \quad (52)$$

3.2.3. Summary

We now summarize the procedures of calculating the heat transfer coefficient hpre for high heat fluxes presented above. First, solve Eqs. (37), (46) and (52) simultaneously for δ_{lv}, p_{vf}, and the saturation distribution. Secondly, using the measured value of the minimum capillary radius given by Eq. (3), to determine the local liquid film thickness $\delta_l(\eta)$ in the cylindrical pore from Eq. (12). Thirdly, obtain T_{wp} and $T_\delta(\eta)$ by solving Eqs. (16) and (32) simultaneously. The heat transfer coefficient can finally be calculated from Eq. (24).

4. Comparison with experiments

We now present the predicted results based on the above analytical model and then compare them with the experimental data. All the computations were based on the thermophysical properties of the glass-water system listed in Table 1 as well as the measured vapor pressure at the exit pvo for a specific heat flux presented in Table 2.

The predicted values of the saturation at the heated surface of the porous structure stop and the length of the two-phase zone δ_{lv} are presented in Table 2. It is seen that when the imposed heat flux is less than 158.25 kW/m^2, s_{top} remains to be 1.00 and the corresponding length of the two-phase zone δ_{lv} is zero. As the heat flux is higher than 158.25 kW/m^2, the saturation begins to drop rapidly while the corresponding length of the two-phase begins to increase. The saturation distributions in the two-phase zone for selected heat fluxes (corresponding to 208.75, 229.23, and 259.58 kW/m^2) are displayed in Fig. 9. As seen from this figure, the saturation is progressively decreased from the interface between the subcooled liquid and the two-phase zone ($s = 1$) toward the exit of the porous structure. Fig. 9 also shows that when the imposed heat flux is increased, the saturation at the top decreases while the length of the two-phase zone becomes longer.

A comparison of the heat transfer coefficient based on the theoretical model (represented by the solid line with cross symbols) and the experimental data (represented by the circular symbols) is illustrated in Fig. 4. It may be relevant to mention that the discrete nature of the predicted heat transfer coefficient was due to the fact that the measured outlet vapor pressure data was not continuous. It is seen that the theoretical results, in terms of magnitude and trends, are in good agreement with the experimental data, the maximum

relative difference between the two being less than 11.2%.

5. Concluding remarks

Experimental results and theoretical modeling on evaporative heat transfer characteristics from a capillary porous structure heated with a permeable heating source at the top were reported in this paper. The experiments show that the system was operating in three typical conditions, depending on its heat loads. For small and moderate heat fluxes, evaporation took place uniformly adjacent the heated surface of the wetted porous structure. For higher heat fluxes, the thermodynamic state of the system consisted of a two-phase zone in the upper portion and a subcooled liquid zone in the lower portion in the porous structure. When the imposed heat flux was further increased, a vapor blanket formed below the heated surface and therefore, the corresponding critical heat flux was reached. The heat transfer coefficient was modeled by simultaneously solving the problem of evaporating capillary meniscus in the pore level and the problem of fluid flow through a porous medium. It is shown that the model is in good agreement with the experimental data, predicting the variations of the heat transfer coefficient with the increasing heating load.

Acknowledgements

This work was supported by Hong Kong RGC Earmarked Research Grant No. HKUST 809/96E.

References

[1] J. Ku, E.J. Kroliczek, W.J. Taylor, R. McIntosh, Functional and performance tests of two capillary pumped loop engineering models, AIAA Paper 86-1248, 1986.

[2] D.R. Chalmers, J.J. Pustay, C.B. Moy, E.J. Kroliczek, Application of capillary pumped loop heat transport systems to large spacecraft, AIAA Paper 86-1295, 1986.

[3] G.P. Peterson, An Introduction to Heat Pipes: Modelling, Testing and Applications, Wiley, New York, 1994.

[4] A. Faghri, Heat Pipe Science and Technology, Taylor & Francis, Washington, DC, 1995.

[5] C.Y. Wang, P. Cheng, Advances in heat transfer, in: J.P. Hartnet, T.F. Irvine, Y.I. Cho, G.A. Greene (Eds.), Multiphase Flow and Heat Transfer in Porous Media, vol. 30, Academic Press, New York, 1997.

[6] E.M. Parmentier, Two-phase natural convection adjacent to a vertical heated surface in a permeable medium, Int. J. Heat Mass Transfer 22 (6) (1979) 849–855.

[7] P. Cheng, A.K. Verma, The effect of subcooled liquid on film boiling about a vertical heated surface in a porous medium, Int. J. Heat Mass Transfer 24 (7) (1981) 1151–1160.

[8] C.Y. Wang, C. Beckermann, A two-phase mixture model of liquid–gas flow and heat transfer in porous media. Part II: Application to pressure-driven boiling flow adjacent to a vertical heated plate, Int. J. Heat Mass Transfer 36 (11) (1993) 2759–2768.

[9] P.S. Ramesh, K.E. Torrance, Boiling in a porous layer heated from below: effects of natural convection and a moving liquid/two-phase interface, J. Fluid Mechanics 257 (1993) 289–309.

[10] C.K. Sondergeld, D.L. Turcotte, An experimental study for two-phase convection in a porous medium with applications to geological problems, J. Geophysics Resources 82 (1977) 2045–2053.

[11] A.S. Demidov, E.S. Yatsenko, Investigation of heat and mass transfer in the evaporation zone of a heat pipe operating by the 'inverted meniscus' principle, Int. J. Heat Mass Transfer 37 (14) (1994) 2155–2163.

[12] D. Khrustalev, A. Faghri, Heat transfer in the inverted meniscus type evaporator at high heat fluxes, Int. J. Heat Mass Transfer 38 (16) (1995) 3091–3101.

[13] V.P. Carey, Liquid–Vapor Phase-Change Phenomena: An Introduction to the Thermophysics of Vaporization and Condensation Processes in Heat Transfer Equipment, Hemisphere, Washington, DC, 1992.

[14] P.C. Wayner Jr, Y.K. Kao, L.V. Lacroix, The interline heat-transfer coefficient of an evaporating wetting film, Int. J. Heat Mass Transfer 19 (1976) 487–492.

[15] K.S. Udell, Heat transfer in porous media heated from above with evaporation, condensation, and capillary effects, ASME J. Heat Transfer 105 (1983) 485–492.

[16] A.K. Verma, K. Pruess, C.F. Tsang, P.A. Withespoon, A study of two-phase concurrent flow of steam and water in an unconsolidated porous medium, ASME HTD 46 (1984) 135–143.

[17] K.A. Grosser, R.G. Carbonell, S. Sundaresan, The onset of pulsing in two-phase co-current downflow through a packed bed, AIChe J 34 (11) (1988) 1850–1860.